

DYNAMICAL TIMESCALE OF PRECOLLAPSE EVOLUTION INFERRED FROM CHEMICAL DISTRIBUTION IN THE TAURUS MOLECULAR CLOUD-1 (TMC-1) FILAMENT

YUNHEE CHOI AND JEONG-EUN LEE

School of Space Research, Kyung Hee University, 1732, Deogyong-daero, Giheung-gu, Yongin-si, Gyeonggi-do 17104, Republic of Korea

TYLER L. BOURKE

Square Kilometre Array Organisation, Jodrell Bank Observatory, Lower Withington, Cheshire SK11 9DL, UK

NEAL J. EVANS II

Department of Astronomy, University of Texas at Austin, 2515 Speedway, Stop C1400, Austin, TX 78712-1205, USA
 Korea Astronomy and Space Science Institute, 776 Daedeokdaero, Daejeon 305-348, Korea

ABSTRACT

We present observations and analysis of the low-mass star-forming region, Taurus Molecular Cloud-1 (TMC-1). CS ($J=2-1$)/N₂H⁺ ($J=1-0$) and C¹⁷O ($J=2-1$)/C¹⁸O ($J=2-1$) were observed with FCRAO (Five College Radio Astronomy Observatory) and SRAO (Seoul Radio Astronomy Observatory), respectively. In addition, *Spitzer* infrared data and 1.2 mm continuum data observed with MAMBO (Max-Planck Millimetre Bolometer) are used. We also perform chemical modeling to investigate the relative molecular distributions of the TMC-1 filament. Based on *Spitzer* observations, there is no young stellar object along the TMC-1 filament, while five Class II and one Class I young stellar objects are identified outside the filament. The comparison between column densities calculated from dust continuum and C¹⁷O 2–1 line emission shows that CO is depleted much more significantly in the ammonia peak than in the cyanopolyne peak, while the column densities calculated from the dust continuum are similar at the two peaks. N₂H⁺ is not depleted much in either peak. According to our chemical calculation, the differential chemical distribution in the two peaks can be explained by different timescales required to reach the same density, i.e., by different dynamical processes.

Keywords: astrochemistry — ISM: individual objects (TMC-1) — ISM: molecules — ISM: abundances

1. INTRODUCTION

Gravitationally bound starless cores, that is, prestellar cores, are cold ($T_k \sim 10$ K), dense ($n > 10^4$ cm⁻³) condensations of gas with no sign of a central protostellar object, implying that they are the earliest identifiable stage of star formation (e.g., Shu et al. 1987; Lee & Myers 1999; Crapsi et al. 2005; Ward-Thompson et al. 2007). Therefore, prestellar cores are the places that we can study the initial conditions of star formation such as the distribution of density, temperature, and velocity (Benson & Myers 1989; Ward-Thompson et al. 1994). Prestellar cores have a constant density in the inner part and a decreasing density at larger radii (Ward-Thompson et al. 1994, 1999, 2000; Andre et al. 1996), which can be well described with a Bonnor-Ebert sphere density profile (Evans et al. 2001). Dust grain temperatures decrease toward the center of prestellar cores (Evans et al. 2001; Zucconi et al. 2001; Ward-Thompson et al. 2002; Crapsi et al. 2007; Harju et al. 2008; Nielbock et al. 2012) since the interstellar radiative field (ISRF) is the only heating sources of prestellar cores.

Although there are several model scenarios to explain core formation, they can be divided into two extreme paradigms: slow quasistatic contraction and dynamic turbulent processes. In the former process, a core gradually becomes condensed toward the center through ambipolar diffusion, increasing the ratio of core mass to magnetic flux. As a core switches from magnetically subcritical to a supercritical condition, the core can collapse gravitationally (Mouschovias 1991; Mouschovias & Ciolek 1999; Shu et al. 1987). If compressible turbulence dominates in a prestellar core, the turbulence will decline in a short time (e.g., Mac Low et al. 1998) and collapse will happen. This means that the prestellar core disappears quickly or rapidly collapses. The detailed modeling results of this process suggest that the cores live for only one or two free-fall times (e.g., Ballesteros-Paredes et al. 2003; Vázquez-Semadeni et al. 2005).

Demographic studies indicate lifetimes that decline with increasing density from near 10 free-fall times at 10^3 cm^{-3} to a few free-fall times, or about 0.5 Myr, once the mean density rises above $2 \times 10^4 \text{ cm}^{-3}$, and one free-fall time once the mean density is above 10^6 cm^{-3} (Ward-Thompson et al. 2007; Enoch et al. 2008; André et al. 2014).

Studies show that the chemical compositions of dark cloud cores can be a useful tracer of their evolutionary status in a given dynamical process, as the chemistry is time dependent. The dynamical evolutionary stage can be inferred by the density structure of a core, which can be obtained through the dust continuum emission. However, one of the important properties of dynamical processes is the velocity distribution, which is traced only by line profiles within the core. Molecular line profiles are affected by not only density and temperature profiles but also the abundance structure in the core. Therefore, it is necessary to understand the chemical distribution within cores (e.g., Mizuno et al. 1990; Zhou et al. 1993; Choi et al. 1995; Bergin et al. 1995; Gregersen et al. 1997; Gregersen & Evans 2000; Mardones et al. 1997; Aikawa et al. 2001; Lee et al. 2003, 2004; Di Francesco et al. 2001; Belloche et al. 2002).

Taurus Molecular Cloud-1 (TMC-1) is an interesting source for exploring the chemistry of dark clouds. It is a cold and dense cloud with a narrow filamentary structure ($5' \times 15'$) in the Taurus dark-cloud complex at a distance of $\sim 140 \text{ pc}$ (Elias 1978; Kenyon et al. 1994; Torres et al. 2012) extending from the southeast to northwest direction, with an infrared source (IRAS 04381+2540) located outside the northwest part. The TMC-1 filament has been observed in many molecular lines. According to those molecular observations, carbon-chain molecules such as CCS, C_4H , and HC_3N are abundant in the southeast part (cyanopolyne peak) of the TMC-1 filament, and NH_3 and N_2H^+ are abundant in its northwest part (ammonia peak). This peculiar chemical feature of TMC-1 has been an interesting problem, so there have been many studies attempting to understand the chemical distributions in TMC-1 (e.g., Churchwell et al. 1978; Little et al. 1979; Wootten et al. 1980; Toelle et al. 1981; Guelin et al. 1982; Snell et al. 1982; Schloerb et al. 1983; Olano et al. 1988; Hirahara et al. 1992; Suzuki et al. 1992; Pratap et al. 1997; Hirota et al. 1998; Markwick et al. 2000, 2001; Saito et al. 2002; Hirota et al. 2003; Suutarinen et al. 2011).

Many studies have concluded that the cyanopolyne peak is at an earlier evolutionary stage than the ammonia peak, and thus the cyanopolyne peak (southeast part) is less chemically evolved than the northwest part based on the chemical models and molecular line observations such as CCS, HC_5N , C^{34}S , NH_3 , C^{34}S , DCO^+ , H^{13}CO^+ , and CH. The estimated chemical evolutionary age difference between the two peaks is more than 10^5 yr (e.g., Suzuki et al. 1992; Hirahara et al. 1992; Hanawa et al. 1994; Howe et al. 1996; Pratap et al. 1997; Saito et al. 2002; Suutarinen et al. 2011).

Hirahara et al. (1992) showed that the H_2 density of the southeast part was lower than that of northwest part by a factor of 10 using C^{34}S . They suggested that the cyanopolyne peak was in an earlier stage of chemical evolution than the ammonia peak because of the higher density at the ammonia peak. Pratap et al. (1997) observed several molecular species and suggested two possibilities for the chemical difference along the TMC-1 filament. One was a small variation in the C/O ratio from 0.4 to 0.5. Another was that differences in density, which varies by a factor of 2 along the filament, could explain the difference of chemical distribution in the TMC-1 filament. The latter was consistent with the result by Hirahara et al. (1992) because the higher density could drive chemical processes more rapidly. Recently, Suutarinen et al. (2011) presented a CH abundance gradient in TMC-1, from $\sim 1.0 \times 10^{-8}$ in the northwestern part to $\sim 2.0 \times 10^{-8}$ in the southeastern part of TMC-1, and they noted that the CH column density peaks close to the cyanopolyne peak. They suggested that the southeastern part in the vicinity of the cyanopolyne peak had an extensive low-density envelope based on the comparison of the dust continuum maps from SCUBA 850 and $450 \mu\text{m}$ (Nutter et al. 2008) and the modelling of molecular lines (Hirahara et al. 1992; Pratap et al. 1997), implying that the cyanopolyne peak was in the early stage of dynamical evolution and this peak was also chemically less evolved than the ammonia peak because of the lower density.

Markwick et al. (2000, 2001) proposed another explanation for molecular abundance differences along the TMC-1 filament. They investigated the possibility that the gradients were produced by spontaneous explosive desorption of UV-photolyzed ice mantles, triggered by the heating of dust grains and their ices, through grain-grain collisions induced by MHD waves from IRAS 04381+2540 near the ammonia peak. The chemical processes occurred first in the ammonia peak and later in the cyanopolyne peak, which induced the gradient of molecular abundances along the TMC-1 filament. According to their chemical models, the ammonia peak is $1.5 \times 10^5 \text{ yr}$ older than the cyanopolyne peak, assuming the speed of the MHD wave of 2 km s^{-1} .

A very different explanation for the chemical distribution along the TMC-1 filament might be possible. According to gas-phase chemical models, carbon-chain species such as CCS form before atomic carbon mainly reacts with atomic oxygen, which drives all carbon-bearing species into CO. When the depletion of CO (and even N_2H^+) is very significant, abundances of carbon-chain species increase again, which is called a late-time secondary abundance peak of carbon-chain species (Ruffle et al. 1997, 1999; Li et al. 2002; Lee et al. 2003). In this case, the cyanopolyne peak might be

Table 1. List of Observed Lines.

Molecule	Transition	Telescope	ν (GHz)	δv (km s ⁻¹)	θ_{mb} (arcsec)	η_{mb}	rms (K)	Observing Date
N ₂ H ⁺	$J=1-0$	FCRAO 14 m	93.174	0.08	58	0.5	0.1	2003 Jan.
CS	$J=2-1$	FCRAO 14 m	97.981	0.07	55	0.5	0.1	2003 Jan.
C ¹⁸ O	$J=2-1$	SRAO 6 m	219.560	0.13	48	0.57	0.04	2009 Feb.
C ¹⁷ O	$J=2-1$	SRAO 6 m	224.714	0.13	48	0.57	0.04	2009 Feb.

chemically older than the ammonia peak, unlike the conclusion from the rest of the studies. Therefore, we need to calculate accurate depletion factors of N₂H⁺ and CO in the two peaks using accurate H₂ column densities.

In this study, we present new data from the FCRAO (Five College Radio Astronomy Observatory) 14-m Telescope and the SRAO (Seoul Radio Astronomy Observatory) 6-m Telescope, along with data from the *Spitzer* Space Telescope and MAMBO (Max-Planck Millimetre Bolometer) at the IRAM 30-m Telescope. We combine these data sets to study the reason for the chemical differentiation along the filament. We determine the degree of molecular depletion by comparing column densities calculated from dust continuum emission and molecular line emission, since the dust continuum at (sub)millimeter traces the total material along the line of sight very well. We also carry out chemical calculations to study the abundance evolution of CO and N₂H⁺ with different assumptions about the evolution of the core densities.

Observations of TMC-1 are summarized in Section 2. In Section 3 we show the observational results and simple analysis. Section 4 presents the column densities using several molecules and dust continuum emission. Section 5 describes the chemical modeling sequence and results. Finally, we discuss our results in Section 6.

2. OBSERVATIONS

2.1. Five College Radio Astronomy Observatory (FCRAO) Observations

Maps of CS ($J=2-1$) and N₂H⁺ ($J=1-0$) toward TMC-1 were made in 2003 January with the 14-m telescope of the Five College Radio Astronomy Observatory (FCRAO). The 32-element heterodyne receiver SEQUOIA was used with the auto-correlator configured with a band width of 25 MHz over 1024 channels. The total mapping times were 237 hours and 130 hours for CS ($J=2-1$) and N₂H⁺ ($J=1-0$), respectively. The reference center of maps was (α , δ)=(4^h41^m44.0^s, +25°42′22.0″).

2.2. Seoul Radio Astronomy Observatory (SRAO) Observations

We observed TMC-1 in C¹⁷O ($J=2-1$) and C¹⁸O ($J=2-1$) with the 6-m telescope of Seoul Radio Astronomy Observatory (SRAO) in 2009 February. The autocorrelator was configured with a band width of 100 MHz over 2048 channels. The pointing uncertainty was less than 10″ in both azimuth and elevation. We observed the positions of the cyanopolyne peak and the ammonia peak in the TMC-1 filament. The total integration time for each position was 30 minutes.

Table 1 summarizes basic observational parameters of the FCRAO and SRAO data, including the frequency (ν), velocity resolution (δv), the FWHM beam size (θ_{mb}), the main beam efficiency (η_{mb}), rms noise level at the given velocity resolution, and the observing date.

2.3. The Spitzer Space Telescope Observations

The *Spitzer* Legacy Program “From Molecular Cores to Planet Forming Disks” (c2d; Evans et al. 2003) observed TMC-1 at 3.6, 4.5, 5.8, and 8.0 μm with the Infrared Array Camera (IRAC; Fazio et al. 2004) on 2004 October 8 and at 24 and 70 μm with the Multiband Imaging Photometer for *Spitzer* (MIPS; Rieke et al. 2004) on 2004 September 25. The pixel sizes are 1″.2 for all IRAC bands and 2″.45 at MIPS 24 μm . These images were centered at (α , δ)=(4^h41^m14^s, +25°59′31″) for the 3.6 and 5.8 μm bands and (4^h41^m19^s, +25°52′49″) for the 4.5 and 8.0 μm bands. MIPS image was centered at (α , δ)=(4^h41^m21^s, +25°55′46″). For detailed descriptions of data reduction refer to Evans et al. (2007).

2.4. Max-Planck Millimetre Bolometer (MAMBO) Observations

The observations of the 1.2 mm thermal dust continuum emission toward TMC-1 were performed with the IRAM 30-m-telescope on Pico Veleta (Spain) using the 117-receiver MAMBO-2 (240″ diameter) camera (Kreysa et al. 1999).

Table 2. Fluxes of Young Stellar Object Candidates in TMC-1.

Source ^a	c2d ID	R.A. (J2000) (h m s)	Dec. (J2000) (° ' ")	Fluxes from 2MASS (mJy)			Fluxes from <i>Spitzer</i> (mJy)					
				J (1.235 μ m)	H (1.662 μ m)	Ks (2.159 μ m)	IRAC1 (3.6 μ m)	IRAC2 (4.5 μ m)	IRAC3 (5.8 μ m)	IRAC4 (8.0 μ m)	MIPS1 (24 μ m)	MIPS2 (70 μ m)
YSO 1	SSTc2d J044049.5+255119	04 40 49.5	25 51 19.1	7.99E+01	1.10E+02	1.06E+02	6.69E+01	6.42E+01	5.54E+01	5.43E+01	5.58E+01	
YSO 2	SSTc2d J044108.2+255607	04 41 08.2	25 56 07.4	5.11E+00	1.42E+01	2.45E+01	3.71E+01	4.11E+01	4.46E+01	5.19E+01	8.64E+01	
YSO 3	SSTc2d J044110.8+255512	04 41 10.8	25 55 11.6	8.42E+00	1.45E+01	1.76E+01	1.32E+01	1.36E+01	1.37E+01	1.59E+01	1.80E+01	
IRAS source ^b	SSTc2d J044112.6+254635	04 41 12.6	25 46 35.4	2.20E-01	2.27E+00	1.61E+01		1.39E+02		3.46E+02	1.72E+03	6.74E+03
YSO 4	SSTc2d J044124.6+254353	04 41 24.6	25 43 53.0	3.30E-01	3.95E+00	1.33E+01	1.95E+01	2.05E+01	2.09E+01	1.94E+01	4.31E+01	
YSO 5	SSTc2d J044138.8+255627	04 41 38.8	25 56 26.8	2.90E+01	9.14E+01	1.39E+02	1.16E+02	1.59E+02	2.48E+02	4.22E+02	1.27E+03	2.11E+03

^aThe numbers refer to the marked YSOs in Fig. 1.

^bIRAS 04381+2540.

The beam size on the sky was 11'', and the effective frequency is 250 GHz with half sensitivity limits at 210 GHz and 290 GHz. TMC-1 was observed between the summer of 2002 and the winter of 2003/2004. The detailed process of the data reduction of MAMBO observations was explained in [Kauffmann et al. \(2008\)](#), where these data were first presented.

3. OBSERVATIONAL RESULTS & BASIC ANALYSIS

We present the relevant data sets in this section, starting with the infrared and submillimeter continuum data, which establish the environmental context for the molecular line observations.

3.1. Infrared Observations

Figure 1 shows 1.2 mm dust continuum emission (contours) on top of the *Spitzer* three-color image (4.5, 8.0, and 24 μ m for blue, green, and red, respectively). The 1.2 mm dust continuum emission shows that the contours around the cyanopolyne peak are complex compared to those around the ammonia peak. The IRAS source (IRAS 04381+2540) marked with a large box, is located in the northwest part of TMC-1. The small boxes represent YSO candidates that are classified in the c2d source catalogs ([Evans et al. 2007](#)). The source identification numbers are assigned with increasing right ascension. With the *Spitzer* observations, we confirm that there are no YSO candidates along the densest part of the TMC-1 filament although 6 YSO candidates (including the IRAS source) are identified outside or at boundary of the TMC-1 filament. There is a gradient in the 4.5 and 8 μ m emission from northwest to southeast direction probably due to IRAS 04380+2553, which is a late B-type star, HD 29647, behind TMC-1 ([Whittet et al. 2004](#); [Mooley et al. 2013](#)). The 4.5 and 8 μ m radiation from HD 29747 is scattered by dust grains in low densities. Therefore, the gradient of the scattered light emission might imply that the TMC-1 filament is inclined toward HD 29647. As a result, the surface of its northwest part is more illuminated by the B star.

To check the evolutionary stages of the 6 YSO candidates we use the same color-color and color-magnitude diagrams (Fig. 2) as used in [Lee et al. \(2006\)](#). The diagrams use the photometric data from the 2MASS (Two Micron All Sky Survey; [Skrutskie et al. 2006](#)), IRAC, and MIPS bands. IRAS 04381+2540 is not included in the color-color diagram since it is not covered by the observations at 3.6 and 5.8 μ m. The coordinates and fluxes from the 2MASS and *Spitzer* observations of these YSO candidates are listed in Table 2. As seen in Fig. 2, the IRAS source is a Class 0/I candidate, and 5 YSO candidates are classified as Class II. We compare our classification to previous results in the literature. 6 YSOs including the IRAS source are in good agreement with previously identified objects in the catalogs of [Gutermuth et al. \(2008, 2009\)](#) and [Rebull et al. \(2010\)](#). Table 3 lists previous studies, our classification, and identifications for 6 YSOs.

We also calculate the bolometric luminosity (L_{bol}) and bolometric temperature (T_{bol}) for these 6 YSO candidates using the observed fluxes (see Table 2). The bolometric luminosity (L_{bol}) is calculated by integrating the spectral energy distributions (SEDs), including far-infrared and sub-millimeter wavelengths by extrapolation.

$$L_{\text{bol}} = 4\pi d^2 \int_0^\infty S_\nu d\nu, \quad (1)$$

where d is the distance to the source and S_ν is the flux as a function of frequency of the source. The bolometric temperature (T_{bol}) is described as the temperature of a blackbody with the same flux-weighted mean frequency as the observed SED and it is calculated using the following equation ([Myers & Ladd 1993](#)):

$$T_{\text{bol}} = 1.25 \times 10^{-11} \frac{\int_0^\infty \nu S_\nu d\nu}{\int_0^\infty S_\nu d\nu} \text{ K}. \quad (2)$$

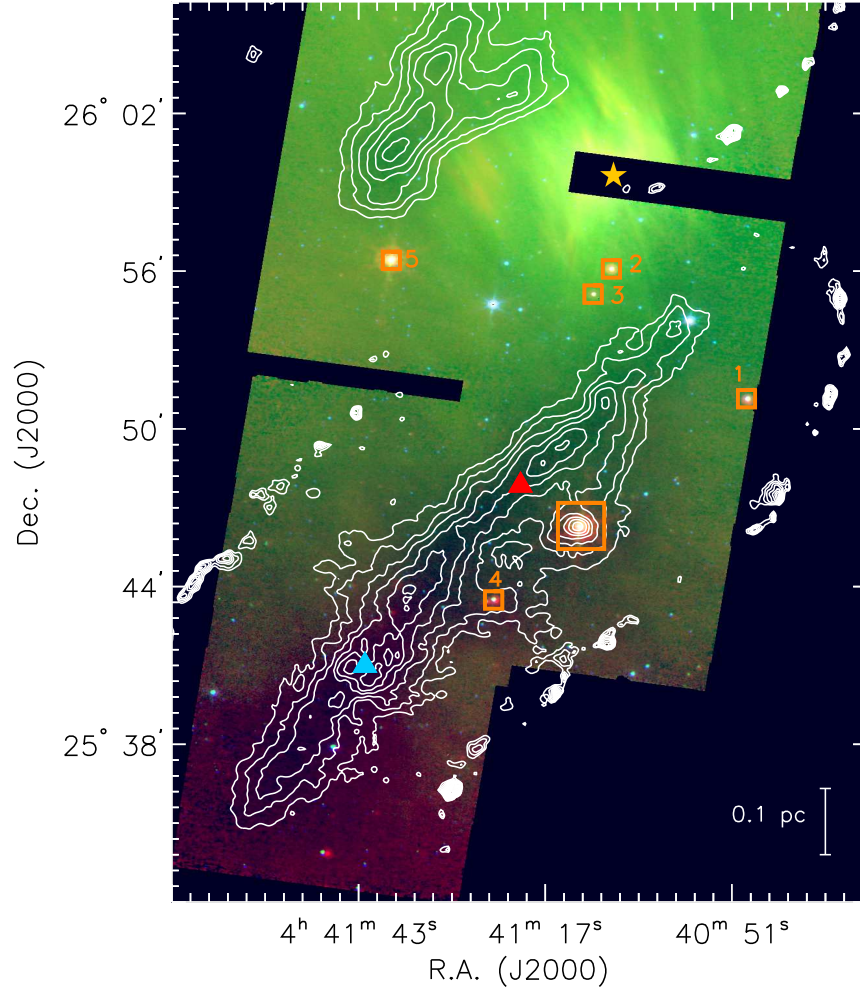


Figure 1. The MAMBO 1.2 mm dust continuum emission (contours) on top of three-color composite *Spitzer* image of TMC-1. The IRAC 4.5 μm , 8.0 μm , and MIPS 24 μm are presented, respectively, as blue, green, and red. The contours begin at 10 mJy beam^{-1} and increase in steps of 5 mJy beam^{-1} . Cyanopolyne peak (blue triangle) and ammonia peak (red triangle) are marked. The large orange box represents IRAS 04381+2540. The small orange boxes indicate classified YSO candidates and they are numbered in order of increasing right ascension. The contours at the top of the image are TMC-1C (Schnee et al. 2007). The yellow star represents the position of HD 29647, but HD 29647 is not shown in this image because the MIPS 24 μm band does not cover the source.

Table 4 shows that the evolutionary stage of each source based on the bolometric temperature (Class I : $70 \text{ K} \leq T_{\text{bol}} \leq 650 \text{ K}$, Class II : $650 \text{ K} < T_{\text{bol}} \leq 2880 \text{ K}$; Chen et al. 1995) is consistent with the result found using the color-color and color-magnitude diagrams. Furthermore, Dunham et al. (2008) calculated the bolometric luminosity and temperature of $\sim 0.73 L_{\odot}$ and $\sim 165 \text{ K}$ for the IRAS source, which is also classified as a Class I object.

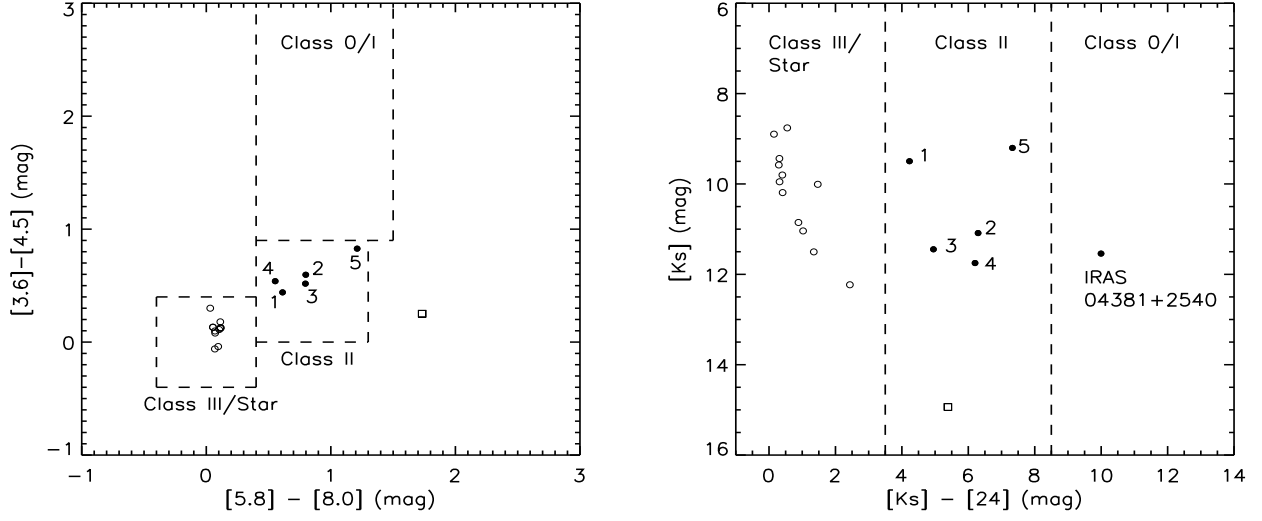


Figure 2. *Left* : Color-color diagram for sources in the IRAC bands ($[3.6]-[4.5]$ vs. $[5.8]-[8.0]$). The filled circles with numbers denote five YSO candidates in TMC-1 (see Fig. 1). The open circles and open square indicate stars and a galaxy, respectively, based on the c2d classification (Evans et al. 2007). The dashed boxes indicate the approximate domains of Class 0/I, Class II, and Class III sources as used in Lee et al. (2006). IRAS 04381+2540 is not included because two IRAC bands (3.6 and $5.8 \mu\text{m}$) do not cover the source. *Right* : Color-magnitude diagram for the 2MASS Ks-band and the MIPS $24 \mu\text{m}$ band sources. This diagram includes IRAS source as well as 5 YSO candidates. The symbols are the same as in the left diagram. The three domains divided by dashed line show different evolutionary stages.

Table 3. Comparison with Previous Studies.

Source ^a	c2d ID	Gutermuth Category ^b	Rebull Category ^c	This Study	Identification ^d
YSO 1	SSTc2d J044049.5+255119	Class II	Class II	II	JH 223
YSO 2	SSTc2d J044108.2+255607	Class II	Flat	II	ITG 33A
YSO 3	SSTc2d J044110.8+255512	Class II	Class II	II	ITG 34
IRAS source	SSTc2d J044112.6+254635	Embedded	Class I	0/I	IRAS 04381+2540
YSO 4	SSTc2d J044124.6+254353	Class II	Flat	II	GKH 32
YSO 5	SSTc2d J044138.8+255627	Class II	Flat	II	Haro 6-33

^aThe numbers refer to the marked YSOs in Fig. 1.

^bGutermuth et al. (2008, 2009)

^cRebull et al. (2010)

^dReference for the first identification of each source: JH 223 - Jones & Herbig (1979); ITG 33A, ITG 34 - Itoh et al. (1999); IRAS 04381+2540 - Beichman et al. (1986); GKH 32 - Gomez et al. (1994); Haro 6-33 - Haro et al. (1953).

Table 4. Results of Bolometric Luminosity and Temperature of 6 YSO Candidates in TMC-1.

Source ^a	c2d ID	$L_{\text{bol}} (L_{\odot})$	$T_{\text{bol}} (K)$	CLASS
YSO 1	SSTc2d J044049.5+255119	0.12	1722	II
YSO 2	SSTc2d J044108.2+255607	0.04	991	II
YSO 3	SSTc2d J044110.8+255512	0.02	1460	II
IRAS source ^b	SSTc2d J044112.6+254635	0.54	214	I
YSO 4	SSTc2d J044124.6+254353	0.02	922	II
YSO 5	SSTc2d J044138.8+255627	0.33	758	II

^aThe numbers refer to the marked YSOs in Fig. 1.

^bIRAS 04381+2540.

3.2. Molecular Line Observations

Figures 3 and 4 present four spectra observed at the cyanopolyne and ammonia peaks. The Gaussian fitting results of CS 2–1 and C¹⁸O 2–1 are obtained using the GILDAS/CLASS package¹ and they are summarized in Table 5. N₂H⁺ 1–0 and C¹⁷O 2–1 have hyperfine structures and they are fitted using the method in the program CLASS (METHOD HFS), which fits the relative intensities of the hyperfine structure lines of a molecular rotational transition to derive the optical depth of the line. The hyperfine fitting results are listed in Table 6. CS 2–1, C¹⁸O 2–1, and the isolated component of N₂H⁺ 1–0, especially at the cyanopolyne peak, show double peaks. This double peak feature could be caused either by optical depth or by two velocity components. Here, we assume that the line shape is caused by optical depth, rather than two velocity components, and fit the data with a single Gaussian.

Figures 5 and 6 present the integrated intensity maps of CS 2–1 (green line) and N₂H⁺ 1–0 (yellow line) obtained at the FCRAO. In the figure, line emissions (contours) are overlaid on the 1.2 mm dust continuum emission map (grey image), and the locations of the cyanopolyne peak and the ammonia peak are denoted by red and blue triangles, respectively. This 1.2 mm dust continuum emission map, the best tracer of column density, is the first 1.2 mm dust continuum emission map of its type for the whole TMC-1 region (Kauffmann et al. 2008). The CS 2–1 intensity does not peak at the cyanopolyne peak, while it peaks close to the ammonia peak. However, the N₂H⁺ 1–0 intensity peaks around both cyanopolyne and ammonia peaks although the intensity close to the cyanopolyne peak is weaker than that around the ammonia peak. The differences of the molecular line intensities at the two peaks can be caused by differences in (1) density, (2) temperature, (3) abundance, or any combinations of these properties.

We use the N₂H⁺ 1–0 line to study the velocity field because that line has the lowest optical depth. Figure 7 presents the first moment map. We found three velocity components; the northern part (red to yellow), the southern part (green), and the northwestern part (sky blue). In the northern part (P1) of the TMC-1 filament, the velocity is $\sim 5.8 \text{ km s}^{-1}$ and it drops to about 5.4 km s^{-1} in the southern part (P5). On the other hand, the source velocity in the northwestern part (IRAS 04381+2540, $V_{\text{LSR}} \sim 5.2 \text{ km s}^{-1}$) is lower than the typical velocity along the TMC-1 filament ($V_{\text{LSR}} \sim 5.6 \text{ km s}^{-1}$), suggesting that this region may be separated from the TMC-1 filament along the line of sight (Toelle et al. 1981; Snell et al. 1982; Kolotovkina et al. 1986; Olano et al. 1988; Fehér et al. 2016).

Table 7 summarizes the source velocities of five positions (P1, P2, P3, P4, and P5) along the TMC-1 filament, consistent with the MAMBO dust continuum peaks (Kauffmann et al. 2008), and the IRAS source (IRAS 04381+2540).

¹ <http://www.iram.fr/IRAMFR/GILDAS/>

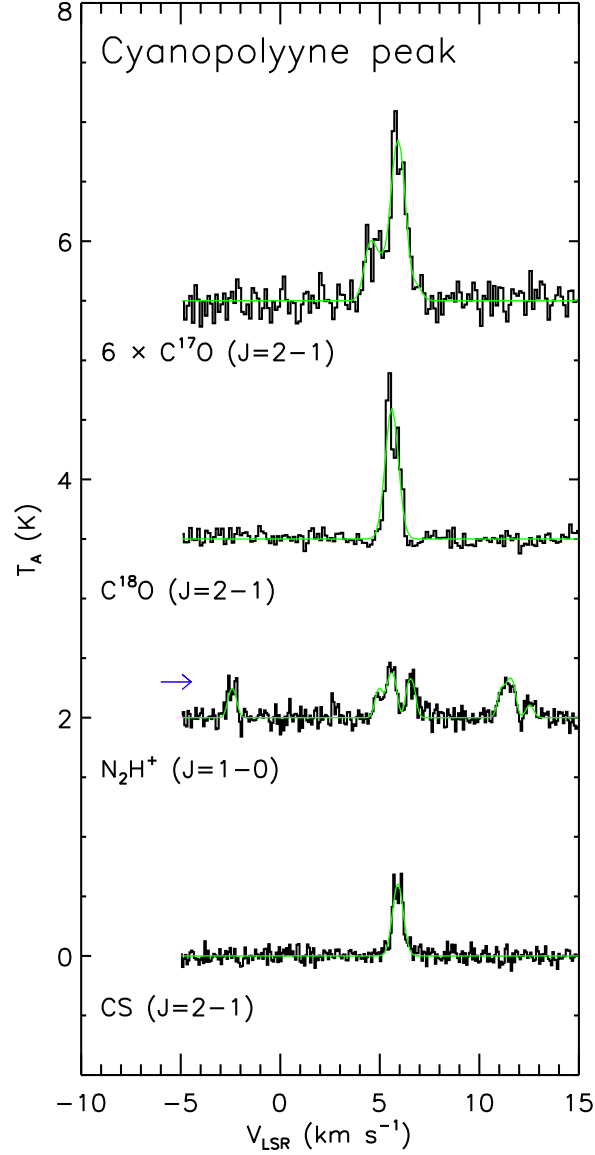


Figure 3. Spectra of molecular transitions observed with the FCRAO 14 m and the SRAO 6 m telescopes at the cyanopolyynes peak (black). The gaussian-fitting results and hyperfine-fitting results for $\text{CS } 2-1/\text{C}^{18}\text{O } 2-1$ and $\text{N}_2\text{H}^+ 1-0/\text{C}^{17}\text{O } 2-1$ are shown as green lines, respectively. The isolated component of $\text{N}_2\text{H}^+ 1-0$ is pointed out by the blue arrow.

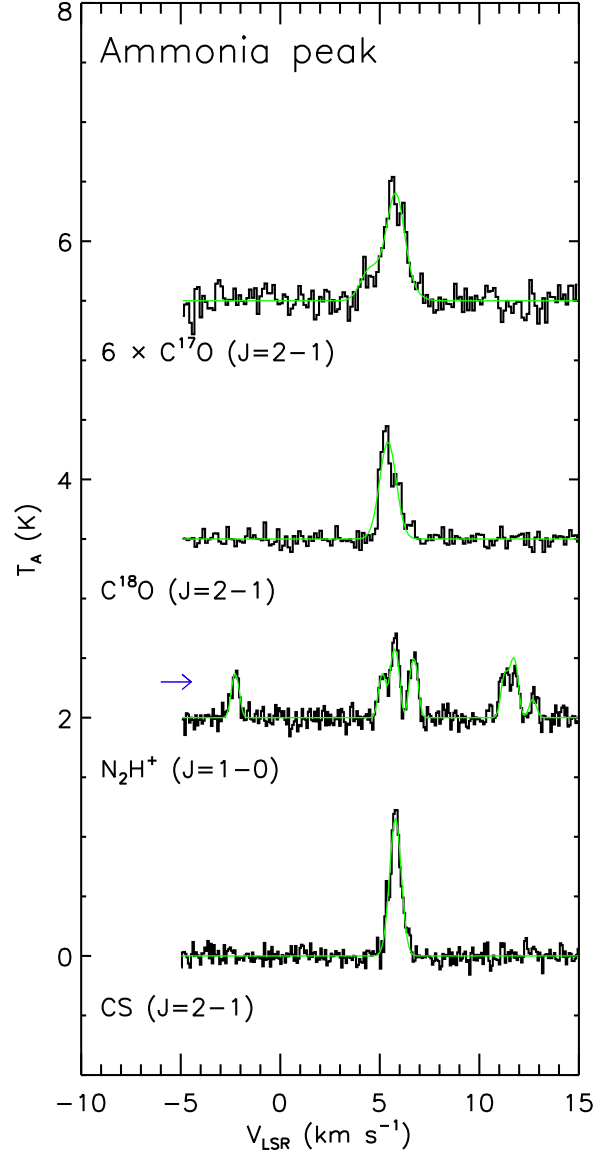


Figure 4. Spectra of molecular transitions observed with the FCRAO 14 m and the SRAO 6 m telescopes at the ammonia peak. The gaussian-fitting results and hyperfine-fitting results for CS 2–1/ C^{18}O 2–1 and N_2H^+ 1–0/ C^{17}O 2–1 are shown as green lines, respectively. The isolated component of N_2H^+ 1–0 is pointed out by the blue arrow.

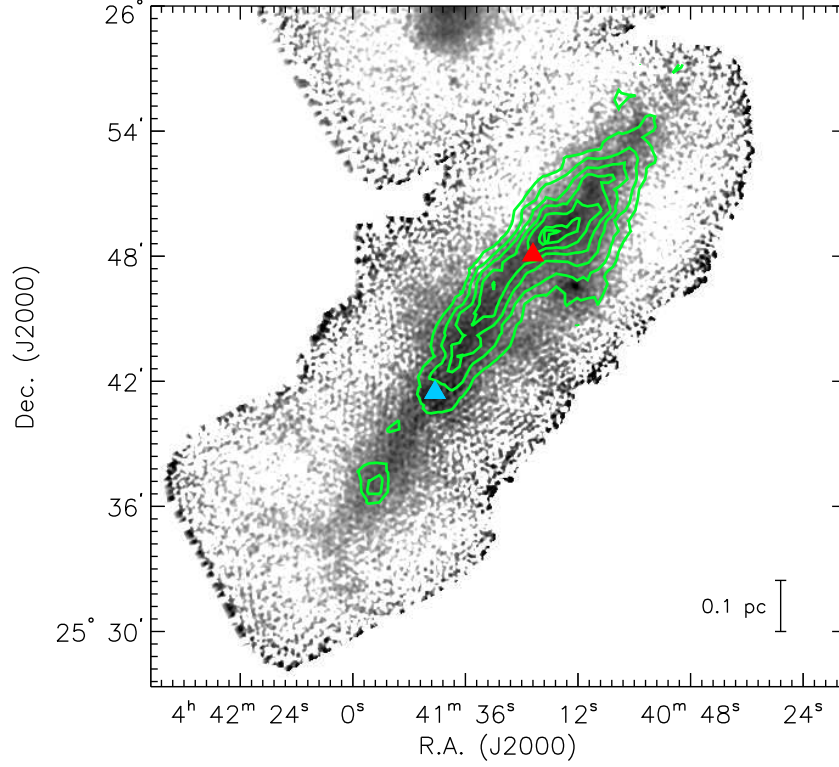


Figure 5. Integrated intensity maps of CS 2–1 (green contours) on top of the 1200 μm dust continuum emission map (gray scale). Blue and red triangles denote the cyanopolyne peak and the ammonia peak, respectively. The contour values are 0.38, 0.53, 0.68, 0.83, 0.98, 1.13, 1.17 K km s^{-1} .

Table 5. Results of Gaussian fits to CS ($J=2-1$) and C^{18}O ($J=2-1$) Lines.

Line	Cyanopolyne Peak				Ammonia Peak			
	V_{LSR} (km s^{-1})	ΔV (km s^{-1})	T_{A} (K)	$\int T_{\text{A}} dV$ (K km s^{-1})	V_{LSR} (km s^{-1})	ΔV (km s^{-1})	T_{A} (K)	$\int T_{\text{A}} dV$ (K km s^{-1})
CS ($J=2-1$)	5.91 (0.01)	0.63 (0.03)	0.60	0.40 (0.01)	5.78 (0.01)	0.70 (0.02)	1.16	0.86 (0.02)
C^{18}O ($J=2-1$)	5.61 (0.01)	0.76 (0.02)	1.08	0.87 (0.01)	5.42 (0.02)	0.94 (0.05)	0.80	0.80 (0.03)

NOTE—The values in parentheses refer to errors of each parameter.

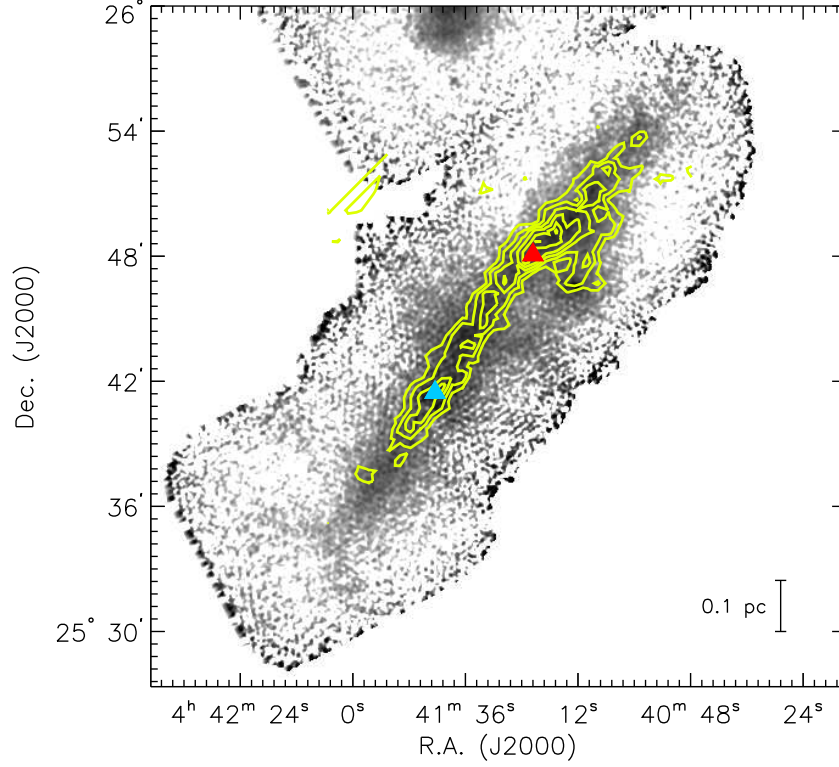


Figure 6. Integrated intensity maps of N_2H^+ 1–0 (yellow contours) on top of the $1200\ \mu\text{m}$ dust continuum emission map (gray scale). Blue and red triangles denote the cyanopolyne peak and the ammonia peak, respectively. The contour values are 0.08, 0.12, 0.16, 0.20, 0.24, 0.27 K km s^{-1} .

Table 6. Results of Hyperfine structure to N_2H^+ ($J=1-0$) and C^{17}O ($J=2-1$) Lines.

Line	Cyanopolyne Peak			Ammonia Peak		
	V_{LSR} (km s^{-1})	ΔV (km s^{-1})	τ^a	V_{LSR} (km s^{-1})	ΔV (km s^{-1})	τ^a
N_2H^+ ($J=1-0$)	5.60 (0.01)	0.44 (0.03)	7.64 (2.11)	5.75 (0.01)	0.41 (0.02)	6.77 (1.63)
C^{17}O ($J=2-1$)	5.65 (0.02)	0.68 (0.05)	1.71 (0.66)	5.53 (0.02)	1.01 (0.04)	0.10 (0.16)

NOTE—The values in parentheses refer to errors of each parameter.

$^a\tau$ is the sum of the optical depths of all hyperfine components.

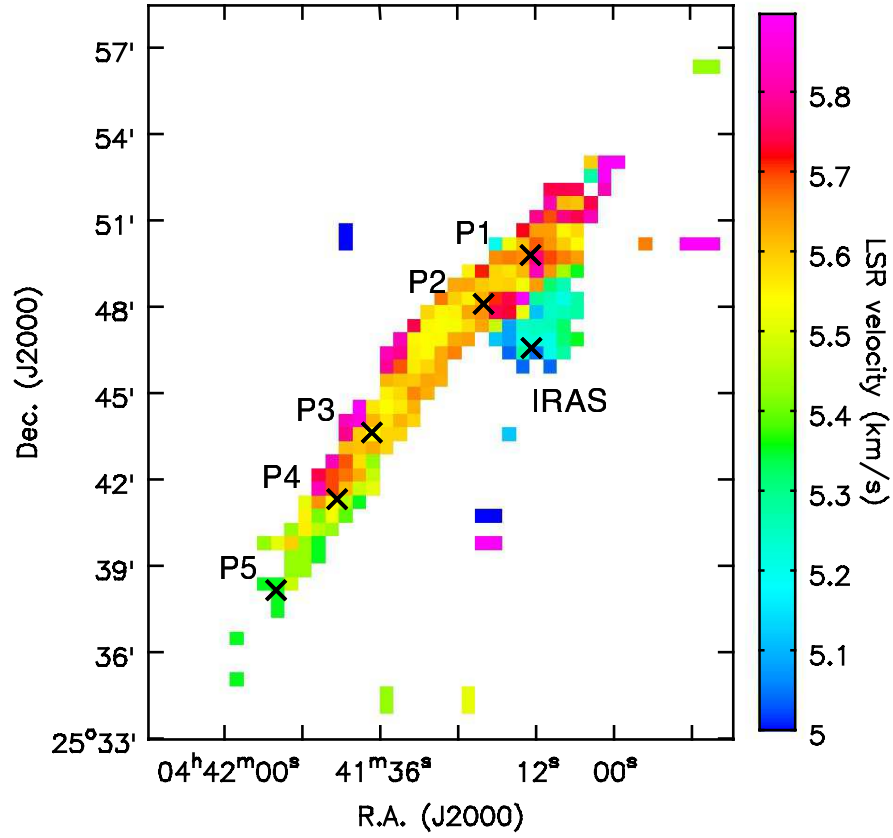


Figure 7. The first moment (i.e., intensity weighted central velocity) map of the N_2H^+ 1–0 line. Five positions (P1, P2, P3, P4, and P5) are placed along the TMC-1 filament in order of increasing right ascension. The IRAS source (IRAS 04381+2540) is shown in the northwest part of the TMC-1 filament. The coordinate and V_{LSR} of each position is listed in Table 7.

Table 7. LSR Velocity in the TMC-1 filament.

Position	R.A. (J2000) (^h ^m ^s)	Dec. (J2000) ([°] ['] ^{''})	LSR Velocity (km s ^{−1})
The direction along the TMC-1 filament			
P1	04 41 13.8	25 49 49.5	5.82 (0.01)
P2 ^a	04 41 20.9	25 48 07.2	5.75 (0.01)
P3	04 41 37.2	25 43 38.5	5.66 (0.01)
P4 ^b	04 41 42.5	25 41 27.0	5.60 (0.01)
P5	04 41 51.9	25 38 09.5	5.42 (0.01)
IRAS ^c	04 41 12.8	25 46 33.5	5.20 (0.01)

NOTE—The values in parentheses refer to errors of LSR velocities.

^aAmmonia peak.

^bCyanoacetylene peak.

^cIRAS 04381+2540.

Table 8. Parameters for Molecules.

Line	Rotational Constant B (MHz)	Dipole Moment μ (D ^a)
N ₂ H ⁺ 1–0	46586.87	3.40
C ¹⁷ O 2–1	56179.99	0.11

NOTE—Molecular spectroscopy data are from the CDMS catalog (Müller et al. 2005, <http://www.astro.uni-koeln.de/cdms>).

^aThe Debye (D) is a unit of the electric dipole moment, 1 D = 10^{−18} g^{1/2} cm^{5/2} s.

4. COLUMN DENSITY CALCULATIONS

4.1. H₂ Column Density from Dust Continuum Emission

We compare H₂ column densities calculated from molecular line emission and dust continuum emission to calculate the degree of depletion of molecules.

If the dust continuum emission is optically thin, the observed flux F_ν^{beam} can be related to the column density of gas. Therefore, we calculate the H₂ column density with the MAMBO flux as given by this equation (Hildebrand 1983).

$$N(\text{H}_2) = \frac{F_\nu^{\text{beam}}}{\Omega_A \mu_{\text{H}_2} m_{\text{H}} \kappa_\nu B_\nu(T)} \quad (3)$$

where F_ν^{beam} is the observed flux per beam, μ_{H_2} (= 2.3) is the molecular weight per hydrogen molecule, m_{H} is the atomic mass unit, κ_ν (= 0.0102 cm²g^{−1}) is the mass opacity of dust per gram of gas at 1.2 mm (Kauffmann et al. 2008), $B_\nu(T)$ is the Planck function, and Ω_A is the beam solid angle; $\Omega_A = (\pi \theta_{\text{HPBW}}^2)/(4 \ln 2)$ for a Gaussian function (Lee et al. 2003; Kauffmann et al. 2008). The MAMBO map is convolved with a Gaussian profile with the FWHM of the beam of molecular observations. As a result, the H₂ column density calculated from dust continuum emission at the cyanopolyne and the ammonia peak is $(1.99 \pm 0.20) \times 10^{22}$ cm^{−2} and $(1.87 \pm 0.19) \times 10^{22}$ cm^{−2}, respectively. The H₂ column densities calculated from the dust continuum emission, the best tracer of the column density along the line of sight, is essentially identical at the two peaks.

Two other recent studies also concluded that the column densities in the ammonia and cyanopolyne peaks are comparable. Suutarinen et al. (2011) estimated the total H₂ column density in the TMC-1 region using the SCUBA 850 and 450 μ m data from Nutter et al. (2008). The derived $N(\text{H}_2)$ are $\sim 1.3 \times 10^{22}$ cm^{−2} and $\sim 1.6 \times 10^{22}$ cm^{−2} at the ammonia peak and the cyanopolyne peak, respectively. In addition, Fehér et al. (2016) used the *Herschel*/SPIRE images to derive the column densities of 3.3×10^{22} cm^{−2} at the ammonia peak and 2.7×10^{22} cm^{−2} at the cyanopolyne peak. These absolute values are different from ours probably because of different beam sizes. However, the very important point of these calculations including ours is that the column densities at the ammonia and cyanopolyne peaks are similar, contrary to suggestions by some previous studies (see Section 1).

4.2. Column Density and Abundance for Molecular Line Emission

Chemical models predict that CO and N₂H⁺ will be anti-correlated because CO destroys N₂H⁺ in the gas phase. Previous observations of pre- and protostellar regions (Bergin et al. 2001; Tafalla et al. 2002; Lee et al. 2003; Di Francesco et al. 2004; Jørgensen et al. 2004; Pagani et al. 2005) confirmed that N₂H⁺ becomes abundant as CO is frozen onto grain surfaces. Therefore, these two molecules together can trace different chemical evolutionary stages of molecular cores. We use the N₂H⁺ and C¹⁷O lines to calculate column densities more accurately because these lines have hyperfine structures. In this calculation, we assume that (1) the dust continuum emission traces all material along a line of sight; (2) dust and gas are well coupled thermally ($T_{\text{d}} = T_{\text{k}} = 10$ K, Pratap et al. 1997); (3) molecular abundances are constant along the line of sight; and (4) all levels are in LTE, following Lee et al. (2003).

For line emission, if a line is optically thin ($\tau < 0$) for the transition $J = J \rightarrow J - 1$ in a linear molecule, the relation between the column density $N(x)$ of molecule x and the integrated intensity of the line is

$$N(x) = \frac{3kQe^{E_J/kT_{\text{ex}}}}{8\pi^3\nu\mu^2J} \int T_R dv \quad (4)$$

where T_{ex} is the excitation temperature above the ground state, and μ is the dipole moment. The frequency (ν), energy above ground (E_J), and the partition function (Q) can be computed from B , the rotational constant.

Table 9. Column Densities and Abundances for Molecular Lines.

Line	Cyanopolyne Peak		Ammonia Peak	
	Column Density ($\times 10^{13} \text{ cm}^{-2}$)	Abundance ($\times 10^{-9}$)	Column Density ($\times 10^{13} \text{ cm}^{-2}$)	Abundance ($\times 10^{-9}$)
N ₂ H ⁺ 1–0	0.5 (0.2)	0.3 (0.1)	0.6 (0.2)	0.3 (0.1)
C ¹⁷ O 2–1	66.5 (26.7)	33.4 (13.9)	25.1 (3.1)	13.4 (2.0)

NOTE—We correct for the optical depth effect to calculate the column density from N₂H⁺ 1–0 and C¹⁷O 2–1. The values in parentheses refer to errors of each parameter.

However, if the optical depth is not negligible, the optical depth effect is corrected for with the equation :

$$N_{\text{thick}} = N_{\text{thin}} \frac{\tau_{\nu}}{1 - e^{-\tau_{\nu}}} \quad (5)$$

Additionally, we calculate the abundance of molecule, $X(x)$, using the H₂ column density calculated from the dust continuum emission.

$$X(x) = \frac{N(x)}{N(\text{H}_2)_{\text{Dust}}} \quad (6)$$

Table 8 summarizes the parameters (the rotational constant B and the dipole moment μ) used for the calculation of the column densities. The optical depths of the N₂H⁺ 1–0 and C¹⁷O 2–1 lines are obtained by the hyperfine fitting method in the CLASS package (see Table 6). We find that C¹⁷O 2–1 is optically thick at the cyanopolyne peak, but optically thin at the ammonia peak. On the other hand, the total optical depth of N₂H⁺ is too large at both peaks to adopt the Eq. 5. Therefore, we use the isolated component (see Fig. 3 and 4) to derived the column density of N₂H⁺ by assuming that the optical depth of each component is proportional to its LTE intensity ratio. The optical depth of the isolated component is 10% of the total optical depth.

The column densities and abundances for molecular lines are listed in Table 9. The column density from C¹⁷O 2–1 is a factor of 2 larger at the cyanopolyne peak than at the ammonia peak. However, there is no significant difference in the column densities of N₂H⁺ 1–0 between the cyanopolyne and the ammonia peaks when the error is considered.

Table 10 represents the depletion factors of C¹⁷O and N₂H⁺ when we compare the calculated abundances with the canonical abundances, $X(\text{C}^{17}\text{O}) = 1.5 \times 10^{-7}$ and $X(\text{N}_2\text{H}^+) = 5.0 \times 10^{-10}$. This canonical abundance of C¹⁷O is obtained by assuming ¹⁶O/¹⁸O of 540, ¹⁸O/¹⁷O of 3.65 (Wilson & Rood 1994; Penzias 1981), and CO/H₂ of 2.7×10^{-4} (Lacy et al. 1994). The canonical abundance of N₂H⁺ is adopted from Johnstone et al. (2010). We find that the depletion of CO is more significant in the ammonia peak (CO depletion factor = 11.9) compared to the cyanopolyne peak (CO depletion factor = 4.5). This suggests that the ammonia peak is more chemically evolved than the cyanopolyne peak. On the other hand, the depletion of N₂H⁺ is almost identical in the two peaks if errors are considered.

Table 10. Depletion Factors of CO and N₂H⁺.

	Depletion Factors ($X_{\text{canonical}}/X_{\text{measured}}$)	
	Cyanopolyne Peak	Ammonia Peak
C ¹⁷ O	4.5 (1.9)	11.9 (1.9)
N ₂ H ⁺	1.8 (0.7)	1.6 (0.6)

NOTE—The values in parentheses refer to errors of depletion factors.

5. CHEMICAL MODELING

We calculate the evolution of chemical abundances of CO and N₂H⁺ molecules to explain the differential chemical distribution along the TMC-1 filament. According to our analysis in the previous section, the cyanopolyne and ammonia peaks have similar column densities calculated from the dust continuum emission while CO is depleted more significantly at the ammonia peak than at the cyanopolyne peak. This trend implies that longer timescales at lower densities are necessary at the ammonia peak during the density evolution since in that condition, N₂ forms more in the

Table 11. Timescale of Density Evolution for Chemical Modeling.

Gas Density ^b (cm ⁻³)	Timescale ^a (yrs)	
	Cyanopolyne Peak Model	Ammonia Peak Model
10 ³	1.0×10 ⁶	1.5×10 ⁶
10 ⁴	1.0×10 ⁵	6.0×10 ⁵
3×10 ⁴	4.0×10 ⁴	4.0×10 ⁴

^aTimescale spent from a given density to the next density. The final density is 10⁵ cm⁻³.

^bGas density with the mean molecular weight of $\mu = 2.3$.

gas and CO is frozen-out more onto grain surfaces, resulting in a high abundance of N₂H⁺ with a significant depletion of CO. Therefore, we calculate the chemical evolution by varying the timescales over which density evolves to account for the observational results.

We adopt the chemical network used in [Lee et al. \(2004\)](#) and the updated N₂ binding energy used in [Chen et al. \(2009\)](#). In the chemical network, the interactions between gas and dust grains (i.e., freeze-out and evaporation of molecules on and off grain surfaces) are included as well as the pure gas chemistry. We assume that the grain surface is coated by water ice and use the same initial elemental abundances as presented in Table 3 of [Lee et al. \(2004\)](#). According to previous studies ([Hirota et al. 1998, 2003](#)), the two peaks have a current density of $\sim 10^5$ cm⁻³. We therefore consider that the densities of the two peaks evolve from 10³ cm⁻³ to 10⁵ cm⁻³ and assume that a core is formed when a density condensation is larger than 10³ cm⁻³, which is the lowest density at which prestellar cores can be identified ([Ward-Thompson et al. 2007](#)). Table 5 lists the timescale of density evolution, i.e., the amount of time spent from each density to the next density until the density of the two peaks reaches 10⁵ cm⁻³ in the models, which fit the observations the best. The densities in the two models gradually increase as time goes by (see Fig. 8). The timescale spent at low densities (until the density reaches 3×10⁴ cm⁻³) is shorter in the cyanopolyne peak model (1.1×10⁶ yrs) than in the ammonia peak model (2.1×10⁶ yrs); the density evolves faster in the cyanopolyne peak model than the ammonia peak model until the density reaches 3×10⁴ cm⁻³.

Figure 8 presents the abundance evolution of CO and N₂H⁺ in the best-fit models for the cyanopolyne peak and the ammonia peak, and the abundances of the two molecules at $n(\text{H}_2)=10^5$ cm⁻³ in the two models are listed in Table 5. During the density evolution, the CO freeze-out occurs in the two models, but it is more significant in the ammonia peak model than the cyanopolyne peak model, as seen in the observations (see Table 10). The abundance of CO in the cyanopolyne peak model is higher than that of CO in the ammonia peak model by a factor of ~ 3 at $n(\text{H}_2)=10^5$ cm⁻³. On the other hand, the N₂H⁺ abundances in the two models are similar at $n(\text{H}_2)=10^5$ cm⁻³; the N₂H⁺ abundance decreases quickly at $n(\text{H}_2)=10^4$ cm⁻³ in the cyanopolyne peak model because of its destruction via abundant CO, while the N₂H⁺ abundance declines slowly in the ammonia peak model because its destroyer, CO, is already depleted at the low density. In the cyanopolyne peak model, the maximum abundance of N₂H⁺ is lower than that in the ammonia peak model because its destruction by CO is more efficient in the cyanopolyne peak model.

According to our modeling, the timescale difference of 1×10⁶ yrs in density evolution is needed in order to explain the chemical differentiation between the cyanopolyne and ammonia peaks; the cyanopolyne peak has a shorter timescale than the ammonia peak. This implies that the core at the ammonia peak forms earlier than the core at the cyanopolyne peak, which is consistent with the suggestion by previous studies; core formation propagated from the ammonia peak to the cyanopolyne peak ([Hanawa et al. 1994](#); [Howe et al. 1996](#); [Markwick et al. 2000, 2001](#); [Saito et al. 2002](#)). However, the current densities of the two peaks are similar. Therefore, once the core at the ammonia peak forms, it might evolve very slowly until the core at the cyanopolyne peak forms and catches up in its density evolution. According to our chemical models combined with the density evolution of cores, the more evolved chemistry at the ammonia peak can be attributed to the longer timescale of density evolution at the peak.

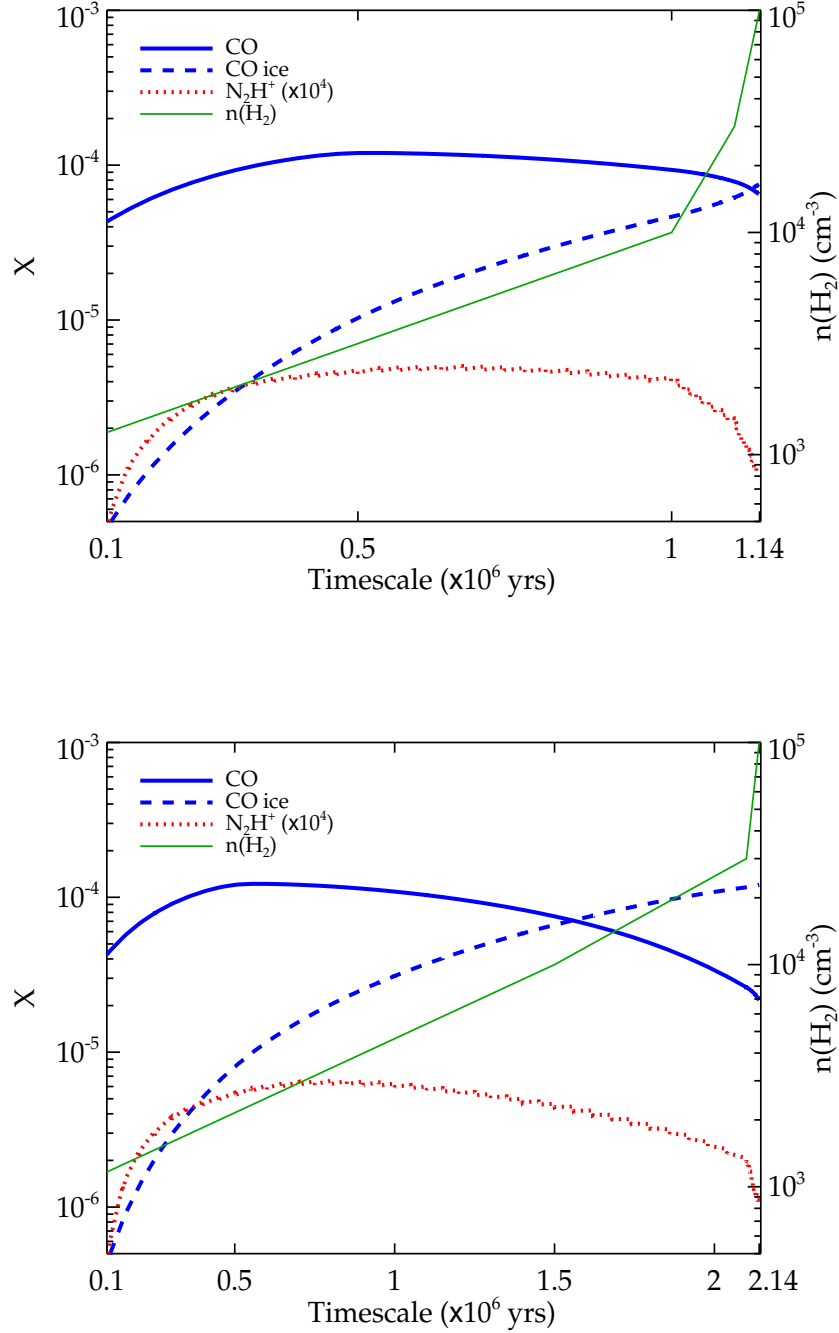


Figure 8. Abundance evolution of CO and N_2H^+ in the cyanopolyne peak model (*upper*) and the ammonia peak model (*lower*) from the chemical calculations. The blue solid and dotted lines represent CO abundances in gas and ice, respectively. The red dotted line indicates the N_2H^+ abundance and the green solid line represents gas density. The timescales until the density reaches 10^5 cm^{-3} are 1.14×10^6 yrs in the cyanopolyne peak model and 2.14×10^6 yrs in the ammonia peak model; the maximum timescales in the horizontal axis are different in two figures.

Table 12. Abundances of CO and N_2H^+ at $n(\text{H}_2) = 10^5 \text{ cm}^{-3}$ in the Chemical Calculation.

Molecule	Abundance	
	Cyanopolyne Peak Model	Ammonia Peak Model
CO ^a	6.50×10^{-5}	2.17×10^{-5}
N_2H^+ ^b	1.06×10^{-10}	1.03×10^{-10}

^aThe maximum CO abundance is 1.2×10^{-4} in both models.

^bThe maximum abundance of N_2H^+ is different in the two models (5×10^{-10} in the cyanopolyne peak model and 6.5×10^{-10} in the ammonia peak model).

Lee et al. (2003) suggested that the chemical evolution of a core depends on its dynamical timescale as well as its density structure by comparing the chemical distributions in three isolated prestellar cores (L1512, L1544, and L1689B). According to Lee et al. (2003), L1544 and L1689B have the same density distribution, but L1689B is chemically much younger than L1544. In conclusion, L1689B might experience a free-fall like dynamical process, while L1544 might undergo an ambipolar diffusion process for the dynamical evolution. In the TMC-1 filament, the core associated with the ammonia peak requires a longer evolutionary timescale, so it would have formed via ambipolar diffusion. On the other hand, the core associated with the cyanopolyne peak might have formed by a more violent dynamical process. Some evidence for the dynamical process on a short timescale is present in our observations. First, the 1.2 mm dust continuum emission, which traces the total amount of material the best, shows a complex structure around the cyanopolyne peak (see Fig. 1). Second, the central velocity of the N_2H^+ line changes sharply around the cyanopolyne peak (see Fig. 7). Finally, the molecular line profiles, especially the isolated component of N_2H^+ $J=1-0$, show a double peak feature (see Fig. 3), indicative of two velocity components. (CS 2–1 and C^{18}O 2–1 are also affected by optical depths.) From this evidence, we could consider that two molecular clouds are colliding around the cyanopolyne peak to induce a fast core formation.

6. SUMMARY

We study a possible interpretation of the differentiated chemical distribution in the TMC-1 region using various observational data and chemical modeling.

From *Spitzer* infrared observations, we confirm that there is no YSO candidates along the TMC-1 filament although there are 6 YSO candidates located outside or at boundary of the TMC-1 filament; five classified YSO candidates objects are classified as Class II sources, and IRAS source (IRAS 04381+2540) is a Class I object, which agree with previous classifications (Dunham et al. 2008; Gutermuth et al. 2008, 2009; Rebull et al. 2010).

The CS 2–1 and N_2H^+ 1–0 lines are stronger at the ammonia peak than at the cyanopolyne peak. On the other hand, C^{17}O 2–1 and C^{18}O 2–1 lines are stronger at the cyanopolyne peak than at the ammonia peak.

Using the C^{17}O and N_2H^+ lines, which have hyperfine structures, we calculate the H_2 column density to compare with the column density calculated from the dust continuum emission, which traces the material the best along the line of sight. The column densities calculated from the dust continuum emission and from the N_2H^+ 1–0 line are similar at the cyanopolyne and ammonia peaks, while the column density calculated from C^{17}O 2–1 is much greater at the cyanopolyne peak than at the ammonia peak.

Comparing the depletion factors of CO and N_2H^+ (see Table 10), we find that the CO molecule is much less depleted at the cyanopolyne peak than at the ammonia peak, while the N_2H^+ abundance is similar at both peaks, ruling out the possibility of a late-time secondary abundance peak of carbon-chain molecules (Ruffle et al. 1997, 1999; Li et al. 2002; Lee et al. 2003) because both CO and N_2H^+ are significantly depleted in the late stage of chemical evolution. Therefore, the relative depletion factors of CO and N_2H^+ imply that the cyanopolyne peak is chemically younger (see Section 1).

According to our chemical modeling, the ammonia peak stays for a longer time at low density (10^3 – 10^5 cm^{-3}) than the cyanopolyne peak to explain the chemical difference between the two peaks, indicating that the dynamical evolution can affect the chemical evolution, resulting in different chemical states even at the same final density. As a result, we suggest that the chemical differentiation along the TMC-1 filament can be induced by different dynamical processes of core formation; the ambipolar diffusion for the ammonia peak and a free-fall like process for the cyanopolyne peak. Some evidence, such as the complex distribution of the 1.2 mm continuum emission (see Fig. 1), the sharp shift of the central velocity of N_2H^+ 1–0 (see Fig. 7), and the double peak feature of molecular line profiles around

the cyanopolyne peak (see Fig. 3) suggest that two molecular clouds are colliding around the cyanopolyne peak to induce a fast core formation.

This research was supported by the Basic Science Research Program through the National Research Foundation of Korea (NRF) (grant No. NRF-2015R1A2A2A01004769) and the Korea Astronomy and Space Science Institute under the R&D program (Project No. 2015-1-320-18) supervised by the Ministry of Science, ICT and Future Planning.

REFERENCES

- Aikawa, Y., Ohashi, N., Inutsuka, S.-i., Herbst, E., & Takakuwa, S. 2001, *ApJ*, 552, 639
- André, P., Di Francesco, J., Ward-Thompson, D., et al. 2014, *Protostars and Planets VI*, 27
- Andre, P., Ward-Thompson, D., & Motte, F. 1996, *A&A*, 314, 625
- Ballesteros-Paredes, J., Klessen, R. S., & Vázquez-Semadeni, E. 2003, *ApJ*, 592, 188
- Beichman, C. A., Myers, P. C., Emerson, J. P., et al. 1986, *ApJ*, 307, 337
- Belloche, A., André, P., Despois, D., & Blinder, S. 2002, *A&A*, 393, 927
- Benson, P. J., & Myers, P. C. 1989, *ApJS*, 71, 89
- Bergin, E. A., Ciardi, D. R., Lada, C. J., Alves, J., & Lada, E. A. 2001, *ApJ*, 557, 209
- Bergin, E. A., Langer, W. D., & Goldsmith, P. F. 1995, *ApJ*, 441, 222
- Chen, H., Myers, P. C., Ladd, E. F., & Wood, D. O. S. 1995, *ApJ*, 445, 377
- Chen, J.-H., Evans, II, N. J., Lee, J.-E., & Bourke, T. L. 2009, *ApJ*, 705, 1160
- Choi, M., Evans, II, N. J., Gregersen, E. M., & Wang, Y. 1995, *ApJ*, 448, 742
- Churchwell, E., Winnewisser, G., & Walmsley, C. M. 1978, *A&A*, 67, 139
- Crapsi, A., Caselli, P., Walmsley, M. C., & Tafalla, M. 2007, *A&A*, 470, 221
- Crapsi, A., Devries, C. H., Huard, T. L., et al. 2005, *A&A*, 439, 1023
- Di Francesco, J., André, P., & Myers, P. C. 2004, *ApJ*, 617, 425
- Di Francesco, J., Myers, P. C., Wilner, D. J., Ohashi, N., & Mardones, D. 2001, *ApJ*, 562, 770
- Dunham, M. M., Crapsi, A., Evans, II, N. J., et al. 2008, *ApJS*, 179, 249
- Elias, J. H. 1978, *ApJ*, 224, 857
- Enoch, M. L., Evans, II, N. J., Sargent, A. I., et al. 2008, *ApJ*, 684, 1240
- Evans, II, N. J., Rawlings, J. M. C., Shirley, Y. L., & Mundy, L. G. 2001, *ApJ*, 557, 193
- Evans, II, N. J., Allen, L. E., Blake, G. A., et al. 2003, *PASP*, 115, 965
- Evans, II, N. J., Harvey, P. M., Dunham, M. M., et al. 2007, *Final Delivery of Data from the c2d Legacy Project: IRAC and MIPS* (Pasadena, CA: SSC)
- Fazio, G. G., Hora, J. L., Allen, L. E., et al. 2004, *ApJS*, 154, 10
- Fehér, O., Tóth, L. V., Ward-Thompson, D., et al. 2016, *A&A*, 590, A75
- Gomez, M., Kenyon, S. J., & Hartmann, L. 1994, *AJ*, 107, 1850
- Gregersen, E. M., & Evans, II, N. J. 2000, *ApJ*, 538, 260
- Gregersen, E. M., Evans, II, N. J., Zhou, S., & Choi, M. 1997, *ApJ*, 484, 256
- Guelin, M., Langer, W. D., & Wilson, R. W. 1982, *A&A*, 107, 107
- Gutermuth, R. A., Megeath, S. T., Myers, P. C., et al. 2009, *ApJS*, 184, 18
- Gutermuth, R. A., Myers, P. C., Megeath, S. T., et al. 2008, *ApJ*, 674, 336
- Hanawa, T., Yamamoto, S., & Hirahara, Y. 1994, *ApJ*, 420, 318
- Harju, J., Juvela, M., Schlemmer, S., et al. 2008, *A&A*, 482, 535
- Haro, G., Iriarte, B., & Chavira, E. 1953, *Boletín de los Observatorios Tonantzintla y Tacubaya*, 1, 3
- Hildebrand, R. H. 1983, *QJRAS*, 24, 267
- Hirahara, Y., Suzuki, H., Yamamoto, S., et al. 1992, *ApJ*, 394, 539
- Hirota, T., Ikeda, M., & Yamamoto, S. 2003, *ApJ*, 594, 859
- Hirota, T., Yamamoto, S., Mikami, H., & Ohishi, M. 1998, *ApJ*, 503, 717
- Howe, D. A., Taylor, S. D., & Williams, D. A. 1996, *MNRAS*, 279, 143
- Itoh, Y., Tamura, M., & Nakajima, T. 1999, *AJ*, 117, 1471
- Johnstone, D., Rosolowsky, E., Tafalla, M., & Kirk, H. 2010, *ApJ*, 711, 655
- Jones, B. F., & Herbig, G. H. 1979, *AJ*, 84, 1872
- Jørgensen, J. K., Hogerheijde, M. R., van Dishoeck, E. F., Blake, G. A., & Schöier, F. L. 2004, *A&A*, 413, 993
- Kauffmann, J., Bertoldi, F., Bourke, T. L., Evans, II, N. J., & Lee, C. W. 2008, *A&A*, 487, 993
- Kenyon, S. J., Dobrzycka, D., & Hartmann, L. 1994, *AJ*, 108, 1872
- Kolotovkina, S. A., Sorochenko, R. L., & Tolmachev, A. M. 1986, *Soviet Astronomy Letters*, 12, 377
- Kreysa, E., Gemünd, H.-P., Gromke, J., et al. 1999, *Infrared Physics and Technology*, 40, 191
- Lacy, J. H., Knacke, R., Geballe, T. R., & Tokunaga, A. T. 1994, *ApJL*, 428, L69
- Lee, C. W., & Myers, P. C. 1999, *ApJS*, 123, 233
- Lee, J.-E., Bergin, E. A., & Evans, II, N. J. 2004, *ApJ*, 617, 360
- Lee, J.-E., Evans, II, N. J., Shirley, Y. L., & Tatematsu, K. 2003, *ApJ*, 583, 789
- Lee, J.-E., Di Francesco, J., Lai, S.-P., et al. 2006, *ApJ*, 648, 491
- Li, Z.-Y., Shematovich, V. I., Wiebe, D. S., & Shustov, B. M. 2002, *ApJ*, 569, 792
- Little, L. T., MacDonald, G. H., Riley, P. W., & Matheson, D. N. 1979, *MNRAS*, 189, 539
- Mac Low, M.-M., Klessen, R. S., Burkert, A., & Smith, M. D. 1998, *Physical Review Letters*, 80, 2754
- Mardones, D., Myers, P. C., Tafalla, M., et al. 1997, *ApJ*, 489, 719
- Markwick, A. J., Charnley, S. B., & Millar, T. J. 2001, *A&A*, 376, 1054
- Markwick, A. J., Millar, T. J., & Charnley, S. B. 2000, *ApJ*, 535, 256
- Mizuno, A., Fukui, Y., Iwata, T., Nozawa, S., & Takano, T. 1990, *ApJ*, 356, 184
- Mooley, K., Hillenbrand, L., Rebull, L., Padgett, D., & Knapp, G. 2013, *ApJ*, 771, 110
- Mouschovias, T. C. 1991, *ApJ*, 373, 169
- Mouschovias, T. C., & Ciolek, G. E. 1999, in *NATO Advanced Science Institutes (ASI) Series C, Vol. 540, NATO Advanced Science Institutes (ASI) Series C*, ed. C. J. Lada & N. D. Kylafis, 305
- Müller, H. S. P., Schlöder, F., Stutzki, J., & Winnewisser, G. 2005, *Journal of Molecular Structure*, 742, 215
- Myers, P. C., & Ladd, E. F. 1993, *ApJL*, 413, L47
- Nielbock, M., Launhardt, R., Steinacker, J., et al. 2012, *A&A*, 547, A11

- Nutter, D., Kirk, J. M., Stamatellos, D., & Ward-Thompson, D. 2008, *MNRAS*, 384, 755
- Olano, C. A., Walmsley, C. M., & Wilson, T. L. 1988, *A&A*, 196, 194
- Pagani, L., Pardo, J.-R., Apponi, A. J., Bacmann, A., & Cabrit, S. 2005, *A&A*, 429, 181
- Penzias, A. A. 1981, *ApJ*, 249, 518
- Pratap, P., Dickens, J. E., Snell, R. L., et al. 1997, *ApJ*, 486, 862
- Rebull, L. M., Padgett, D. L., McCabe, C.-E., et al. 2010, *ApJS*, 186, 259
- Rieke, G. H., Young, E. T., Engelbracht, C. W., et al. 2004, *ApJS*, 154, 25
- Ruffle, D. P., Hartquist, T. W., Caselli, P., & Williams, D. A. 1999, *MNRAS*, 306, 691
- Ruffle, D. P., Hartquist, T. W., Taylor, S. D., & Williams, D. A. 1997, *MNRAS*, 291, 235
- Saito, S., Aikawa, Y., Herbst, E., et al. 2002, *ApJ*, 569, 836
- Schloerb, F. P., Snell, R. L., & Young, J. S. 1983, *ApJ*, 267, 163
- Schnee, S., Caselli, P., Goodman, A., et al. 2007, *ApJ*, 671, 1839
- Shu, F. H., Adams, F. C., & Lizano, S. 1987, *ARA&A*, 25, 23
- Skrutskie, M. F., Cutri, R. M., Stiening, R., et al. 2006, *AJ*, 131, 1163
- Snell, R. L., Langer, W. D., & Frerking, M. A. 1982, *ApJ*, 255, 149
- Suutarinen, A., Geppert, W. D., Harju, J., et al. 2011, *A&A*, 531, A121
- Suzuki, H., Yamamoto, S., Ohishi, M., et al. 1992, *ApJ*, 392, 551
- Tafalla, M., Myers, P. C., Caselli, P., Walmsley, C. M., & Comito, C. 2002, *ApJ*, 569, 815
- Toelle, F., Ungerechts, H., Walmsley, C. M., Winnewisser, G., & Churchwell, E. 1981, *A&A*, 95, 143
- Torres, R. M., Loinard, L., Mioduszewski, A. J., et al. 2012, *ApJ*, 747, 18
- Vázquez-Semadeni, E., Kim, J., Shadmehri, M., & Ballesteros-Paredes, J. 2005, *ApJ*, 618, 344
- Ward-Thompson, D., André, P., Crutcher, R., et al. 2007, *Protostars and Planets V*, 33
- Ward-Thompson, D., André, P., & Kirk, J. M. 2002, *MNRAS*, 329, 257
- Ward-Thompson, D., Kirk, J. M., Crutcher, R. M., et al. 2000, *ApJL*, 537, L135
- Ward-Thompson, D., Motte, F., & Andre, P. 1999, *MNRAS*, 305, 143
- Ward-Thompson, D., Scott, P. F., Hills, R. E., & Andre, P. 1994, *MNRAS*, 268, 276
- Whittet, D. C. B., Shenoy, S. S., Clayton, G. C., & Gordon, K. D. 2004, *ApJ*, 602, 291
- Wilson, T. L., & Rood, R. 1994, *ARA&A*, 32, 191
- Wootten, A., Bozyan, E. P., Garrett, D. B., Loren, R. B., & Snell, R. L. 1980, *ApJ*, 239, 844
- Zhou, S., Evans, II, N. J., Koempe, C., & Walmsley, C. M. 1993, *ApJ*, 404, 232
- Zucconi, A., Walmsley, C. M., & Galli, D. 2001, *A&A*, 376, 650